JET-P(96)47

Collective Thomson Scattering of Millimetre Waves in JET

H Bindslev, J Egedal, J Fessey, J Hoekzema, T Hughes.

JET Joint Undertaking, Abingdon, Oxfordshire, OX14 3EA, UK.

Preprint of a submitted for publication in the Proceedings of the
3rd International Workshop on Strong Microwaves in Plasmas

September 1996

COLLECTIVE THOMSON SCATTERING OF MILLIMETRE WAVES IN JET

H Bindslev, J Egedal, J Fessey, J Hoekzema, T Hughes

JET Joint Undertaking, Abingdon, UK

Abstract

Initial results from The JET Collective Thomson Scattering diagnostic are presented along with estimates of its full diagnostic capability. It is shown that for diagnosis of alpha particle distributions electron cyclotron emission (ECE) received via wall reflections must be reduced by installation of a viewing dump and that at the highest temperatures down shifted ECE radiation in direct view of the receiver is a serious limitation. Finally it is shown that significant anisotropies must be expected in the distributions of thermo–nuclear fusion products. Methods of diagnosing such anisotropies are being considered.

1 Introduction

The JET Collective Thomson Scattering (CTS) diagnostic is expected to be fully operational shortly, providing spatially resolved measurements of the fusion alpha particle and other fast ion velocity distributions. During initial short pulse operation the bulk ion feature was observed, with traces of ICRH driven tails. The signal to noise ratios were in good agreement with theory, indicating that, when fully operational, the diagnostic should be able to measure fast ion distributions.

A 500 kW, 140 GHz gyrotron generates the probing radiation. The frequency of 140 GHz was chosen because the spectrum of scattered light remains sensitive to the fast ion distribution at relatively large scattering angles, refraction is tolerable and a source with sufficiently high power and long pulse length was available. The injected power has to be modulated to discriminate between the scattered radiation and the much brighter (by 2 to 3 orders of magnitude) background radiation from electron cyclotron emission (ECE). Fluctuations on the background radiation are the main source of noise. For standard plasmas with toroidal magnetic fields of 3.4 Tesla, ECE at 140 GHz emanates primarily from the inner and outer edges of the plasma where 140 GHz corresponds to the fundamental and second harmonic of the cyclotron frequency respectively. The ECE background is consequently at a minimum at the probing frequency. The launch and receive antennas, placed at top and bottom of the torus respectively, can both be rotated about two axes providing variable scattering geometry and permitting the localized measurement to be shifted spatially.

2 Diagnostic system

A schematic overview of the diagnostic is given in Figure 1. Only a brief description is given here with emphasis on the initial performance. A more detailed description of the system can be found in COSTLEY ET AL. (1988) and HOEKZEMA ET AL. (1992, 1993).

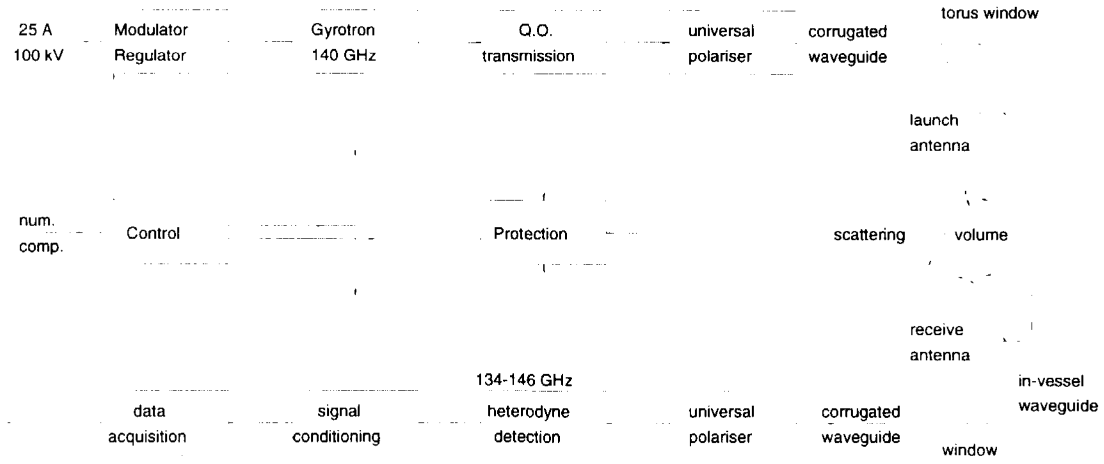

Figure 1: Schematic overview of the diagnostic

The gyrotron can generate 500 kW RF at 140 GHz for 0.5 s. It is important that the RF output is spectrally clean (i.e. power in spurious frequencies in the spectral range of interest > 80 dB down on power in the main frequency) because radiation in spurious frequencies, entering the receiver as stray light, cannot be discriminated from scattered radiation. Spurious frequencies were observed during switch-on and switch-off but not during the flat top of the pulse except at the highest power levels. For the initial operation the gyrotron was switched on at 120 Hz for a number of pulses of 1 ms duration.

The output of the gyrotron is mainly (> 90%) in a Gaussian beam. The high power transmission line (Figure 2) uses a combination of quasi-optical and waveguide propagation. The first part of the transmission system is quasi-optical. Most of the non-Gaussian power is lost from the beam in this section which includes a polariser to produce the desired elliptical polarisation to couple to either the Ordinary or the eXtraordinary mode in the plasma. The Gaussian beam is then coupled into oversized (ID 88.9 mm) corrugated waveguide in which the radiation propagates in the $HE_{1,1}$ mode. Proper alignment of the beam into the waveguide and of the waveguide itself is crucial to avoid significant mode conversion, which would affect the quality of the beam at the end of the waveguide.

With correct alignment, the transmission efficiency of the 60 m. long waveguide run, which includes 7 mitre bends, was extremely good and the burn pattern on thermosensitive paper at the end of the waveguide was closely Gaussian. The RF power level at the torus was about 370 kW.

The last part of the high power transmission line is again quasi optical and a focused

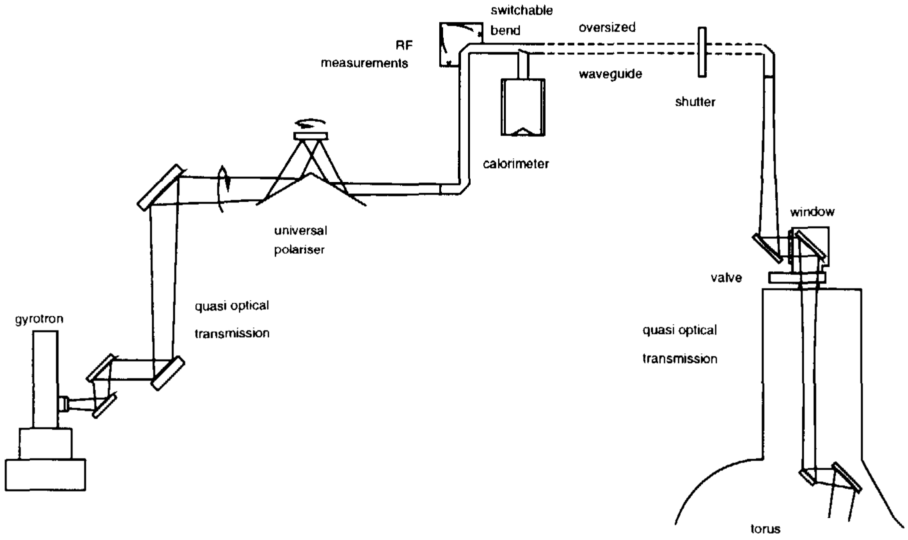

Figure 2: The high power 140 GHz transmission system

Gaussian beam, with a waist radius of 30 mm at the plasma centre, is launched into the torus via a steerable mirror from a top port. For the antenna orientations used in the first measurements, only about 10 mW was coupled to the receiver as stray light.

The receive beam also has a waist radius of 30 mm in the plasma centre and the spatial resolution for the measurement is therefore around 100 mm, dependent on the chosen scattering angle. Via a steerable mirror, the receive beam is focused into corrugated waveguide, which initially has a small diameter (ID 10 mm) to allow curvature around the divertor systems in the bottom of the torus. It is tapered up to 31.75 mm in the bottom port and is continued for $\approx$ 40 m to the detection system where the radiation is coupled into fundamental waveguide via a polariser. The attenuation in the main receive waveguide run is only a few dB. For the initial experiments, relative calibration was obtained by assuming the radiation from the plasma (ECE) is constant in the spectral range of interest and approximate absolute calibration by comparing these signals with those measured by a calibrated ECE diagnostic (although this has a different viewing line through the plasma). Optimum overlap of emitter and receiver beam patterns was established by scanning the main receiver beam from shot to shot. Before the detection system, 2 fundamental waveguide notch filters in series removed the stray light. The stray light attenuation at the centre frequency was at least 80 dB and the full notch width 200 MHz at -3 dB. The heterodyne detection system measures the spectrum between 134 and 146 GHz in 32 channels. The channel bandwidth is chosen to be proportional to the frequency shift. For the measurement of the thermal ion feature only 10 channels closest to the central frequency are of interest. Of these, calibration of the most central 2 or 3 channels is somewhat uncertain due to the effect of the notch filters.

2.1 Results

For the initial measurement the O-mode was selected both for injection and detection. Ray tracing calculations were done to calculate the required antenna directions and polariser settings for an expected plasma. The scattering volume was placed in the centre of the plasma and a scattering vector $|k| = 1500\,\mathrm{m}^{-1}$ was chosen. The scattering angle $\theta = \angle(\mathbf{k}^{\mathrm{i}}, \mathbf{k}^{\mathrm{s}}) = 32°$ while $\phi = \angle(\mathbf{k}^{\delta}, \mathbf{B}) = 122°$. $\mathbf{k}^{\mathrm{i}}$ and $\mathbf{k}^{\mathrm{s}}$ are the wave vectors of the incident and scattered radiation respectively. In operation, only the viewing direction of the receiver beam was adjusted to optimise the overlap. The scattering geometry is slightly different for different plasma parameters, due to the effect of refraction, and was recalculated using the actual plasma parameters. In practice, optimum overlap of the launch and receive beams was lost whenever the plasma magnetic configuration or the density was significantly changed. Generally, a number of similar plasmas were required to optimise the overlap. It should be easier to find the optimum overlap when the slave receivers are operational.

Clear scattering signals were seen from plasmas with $B_0 > 3$ T [HOEKZEMA ET AL. (1995)]. A sample of the raw data is given in Figure 3. These data were taken shortly after a sawtooth collapse. It is seen that the background radiation is going down (cooling of the outer region where this radiation is emitted) while the scattering signal goes up (re-heating of the central region where the scattering volume is located). For this particular discharge, the scattered radiation in the centremost channels was higher than expected, indicating there may still be an effect of scattering off non-thermal fluctuations up to a frequency shift of 100 MHz.

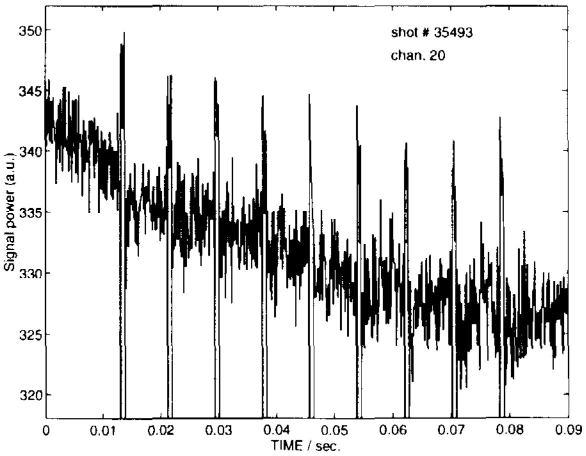

Figure 3: Raw data at $\Delta\nu \approx 600$ MHz from a plasma with $B = 3.1$ T, $n_e = 3 \times 10^{19}\mathrm{m}^{-3}$, $T_e = T_i = 3$ keV, 1.4 MW hydrogen minority heating (ICRH). Nine 1 ms pulses are injected at 120 Hz.

It is also clearly seen from Figure 3 that during switch-on and switch-off of the gyrotron the receiver is saturated. This is due to spurious frequencies generated during switch-on and switch-off which are outside the notch and enter the receiver as stray light. In some channels, at frequencies where spurious signals are present, positive spikes are seen during these periods. Although the receiver seems to recover quickly from these spikes, detailed analysis shows that there are still some saturation effects during the gyrotron pulse. It is possible that this is due to a relatively high power level at frequencies where the detection system is blind, i.e. at frequency shifts around 50 MHz where the notch filters start to transmit. For fast ion measurements, when much smaller scattering signals have to be detected, it will be important to avoid these effects (by using a wider notch filter and clipping the power during switching). At magnetic field values below 3 T no clear scattering signals were found. This was expected since 2nd harmonic absorption starts to interfere around 3 T.

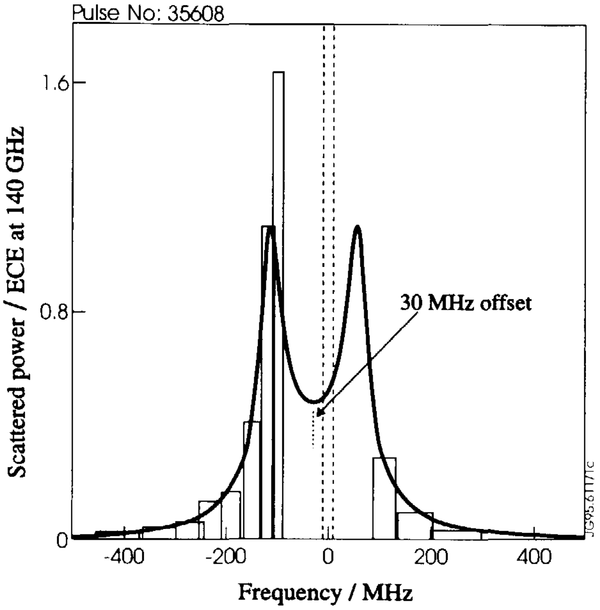

Figure 4: Spectral intensity of scattered light normalized to spectral intensity of ECE at 140 GHz. Shot # 35608 at 57.5 sec. with 5 MW ICRH, $T_{\mathrm{ECE}} = 325$ eV. **Histogram**: Measured signal integrated over 2 gyrotron pulses (1.6 ms).
Curve: theoretical fit. Given: $B = 3.1$ T, $n_e = 4.1 \times 10^{19}\mathrm{m}^{-3}$, $T_e = 3.0$ keV. $\theta = 32°$, $\phi = 122°$. Fitted: $n_{D1} = 1.2 \times 10^{19}\mathrm{m}^{-3}$, $T_{D1} = 3$ keV, $n_{D2} = 0.8 \times 10^{19}\mathrm{m}^{-3}$, $T_{D2} = 20$ keV, $n_N = 0.3 \times 10^{19}\mathrm{m}^{-3}$, $T_N = 3$ keV.

An example of a scattering spectrum is given in Figure 4. The histogram represents the measured spectral intensity in each channel normalised to that of ECE at 140 GHz, which in this case was at a rather low level of 325 eV (for comparison, the alpha feature will only have a radiation temperature of a few eV). A theoretical fit is also given, based on B, n_e and T_e values from other diagnostics while the ion parameters are fitted. The fit is only illustrative. It assumes that the central peaks are due to Nitrogen. The shift of ≈ 30 MHz could be induced by a toroidal drift velocity of 1.6×10^5 m/s. Power accountability is quite good (although the absolute calibration is only approximate): The absolute level of the measured spectral intensity is $\approx 70\%$ of that predicted by theory for perfect beam overlap. The post detection signal to noise ratio, defined as the ratio of the scattered signal to the fluctuations on the total signal, varies over the spectrum between ≈ 10 and ≈ 100. Similar values are found for other spectra.

3 Assessing diagnostic capability of the JET CTS

Collective Thomson Scattering (CTS) spectra, while sensitive to the distribution of fast ions, depend on a wide range of plasma parameters. In the presence of noise in the measured spectra, these do not provide sufficient information to estimate all the relevant parameters with acceptable accuracy; indeed *masking*, where certain variations in parameters lead to no change in the predicted spectrum, makes it impossible to settle the parameters without imposing external constraints, even in the most ideal conditions. These constraints can take the form of parameters measured by other diagnostics or estimated on the basis of theoretical considerations. When assessing whether it is possible to resolve a certain feature, in for instance the fast ion distribution, it is not sufficient that the spectrum be sensitive to this feature, there must not be any other unconstrained perturbation of parameters which gives rise to the same spectral variation. Such masking would lead to large uncertainties in the estimate of the particular feature. Inaccuracies in the constraints can significantly affect the diagnostic capability of CTS, and must be accounted for when analyzing data and assessing diagnostic capability.

Extraction of fast ion distributions and other plasma parameters from CTS spectra is generally done by some fitting procedure. For the best use of the data this fitting should be based on a maximum likelihood estimator which takes into account not only the spectral noise but also uncertainties in constraints. Such an estimator was presented in BINDSLEV (1995) and discussed in detail in BINDSLEV (1996 b). The spectral noise and uncertainty in constraints gives rise to uncertainties in the estimated parameters. This uncertainty can be represented by an error distribution in the space of estimated parameters, which can be visualized as the normalized density of an ensemble of estimates. Directions in which the distribution is narrow are well determined parameter combinations while directions in which it is wide are poorly determined. The best resolved feature in the fast ion distribution corresponds to the direction in parameter space in which the error distribution for the fast ion parameters is narrowest. This is the direction of the first principal component of the distribution. The next best resolved feature, statistically independent of the first, is represented by the direction of the second principal component, etc. The directions and variances of the principal components of the error distribution provide a complete set of independently estimated features and associated uncertainties, and thus provides considerable insight into the diagnostic capability of the system. A detailed analysis of the diagnostic capability of CTS and other complex diagnostics can be based on the error distribution and its principal components, and their relation to noise and uncertainties. We will employ some of these relations here but for a more detailed discussion of the method and its applications the reader is referred to BINDSLEV (1996 b). A brief discussion of the underlying mathematics is also given in BINDSLEV (1995, Section 4).

3.1 Principal components and L_α

In this analysis we base theoretical predictions of the spectral intensity of the received scattered light, $\partial P^{\mathrm{s}}/\partial \nu^{\mathrm{s}}$, on the equation of transfer [BINDSLEV, 1993],

$$\frac{\partial P^{\mathrm{s}}}{\partial \nu^{\mathrm{s}}} = P^{\mathrm{i}} O_b (\lambda_0^{\mathrm{i}})^2 r_e^2 n^{(0)} \Sigma , \tag{1}$$

where the scattering function, Σ, [BINDSLEV, 1996 a] depends on the scattering geometry and plasma parameters.

A realistic list of parameters on which the JET CTS spectra depend is given by the set in Table 1 and parameters describing the fast ion distribution (the list could be extended arbitrarily by assuming more complicated plasma conditions). In the present study we assume that the parameters in Table 1 are constrained with the uncertainties given there.

Constrained parameter		Δ	σ
θ	scattering angle	90°	0.02
ϕ	$\angle(\mathbf{k}^\delta, \mathbf{B})$	90°	0.02
ψ	see caption	90°	0.02
B	$\lvert\mathbf{B}\rvert$, modulus of magnetic field	1 Tesla	0.1
n_e	electron density	$4.5 \times 10^{19} m^{-3}$	0.1
T_e	electron temperature	12 keV	0.05
N_i	n_i/n_e, normalized carbon density	0.03	0.3
R_T	$n_T/(n_d + n_T)$, fuel ratio	0.5	0.3
T_i	bulk ion temperature	10 keV	0.2
O_b	beam overlap	5.8 ($\theta = 20°$)	0.5
$f_{\alpha i}$	$f_\alpha(v_i)$, $i = 0, \ldots, 3$	$f_{\alpha i}$	0.5

Table 1: Set of constrained parameters. Δ is the dynamic range of the parameter and σ is the uncertainty of the constrained parameter relative to its dynamic range. ψ = azimuthal angle of $\mathbf{B}^{(0)}$ when $\hat{\mathbf{z}} \parallel \mathbf{k}^\delta$ and $\hat{\mathbf{x}} \parallel \mathbf{k}^{\mathrm{i}} \times \mathbf{k}^{\mathrm{s}}$. $f_\alpha(v) = f_\alpha(0)/(1 + (v/v_c)^3)$, is the classical slowdown distribution with $v_c = 0.09 \times (T_e/2m_e)^{1/2}$. $v_i = (i/14) \times v_b$, where v_b is the birth velocity. O_b is a measure of the extent to which the emitter and receiver beam patterns overlap.

In addition to the constraints given in Table 1 the bulk ion species (deuterium, tritium and impurity ions) are assumed to have the same temperature, the alpha particle distribution, f_α, is assumed to be isotropic and features in f_α occurring on velocity scales less than $v_b/7$ are ignored. The free parameters are those which describe the alpha particle distribution, excluding the low energy range which is masked by uncertainties in the bulk ion feature. For the numerical analysis the parameters in Table 3.1 are used. These parameters are at present the best estimate of the conditions expected for the coming deuterium, tritium experiments.

parameter	value
θ	10° to 30°
ϕ	80°
ψ	0°
B	3.4 Tesla
n_e	$4.5 \times 10^{19} m^{-3}$
T_e	12 keV
N_i	0.03
R_T	0.5
T_i	20 keV
N_α	3×10^{-3}
$f_{\alpha i}$	$f_\alpha(v_i)$, $i = 0, \ldots, 14$
E_m	4 MeV
P^{i}	400 kW
O_b	$18.8 m^{-1}/\lvert\sin(\theta)\rvert$

Table 2: Parameters used in numerical analysis of diagnostic potential. $N_\alpha = n_\alpha/n_e$ is the normalized alpha density, P^{i} is the power into the plasma. $f_\alpha(v) = f_\alpha(0)/(1 + (v/v_c)^3)$. $v_c = 0.09 \times (T_e/2m_e)^{1/2}$. $v_i = (i/14) \times v_b$, $v_b = (E_b/2m_\alpha)^{1/2}$, $E_b = 3.5\mathrm{MeV}$

To investigate which departures of the fusion alpha particle distribution from the classical slowdown distribution can be detected with JET's CTS, the principal components of the error distribution for the free alpha parameters were computed.

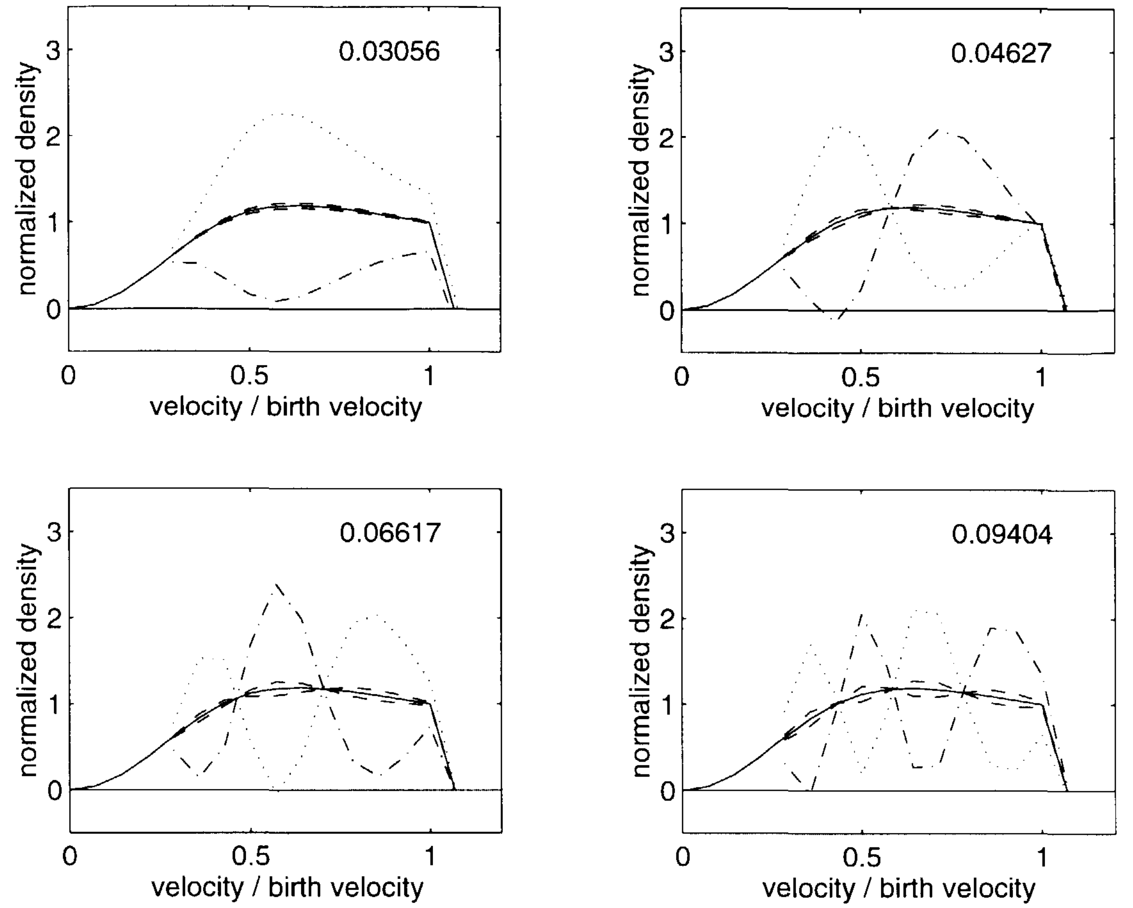

Figure 5: Principal components of alpha particle distribution perturbations. In each subfigure the central solid line is the unperturbed classical slowing down distribution integrated over a surface of constant velocity ($(v/v_b)^2 \times f_\alpha(v)/f_\alpha(0)$). The dotted and dash–dotted lines above and below the central line are respectively the classical distribution plus and minus the perturbation represented by the dynamic range along the particular principal component while the dashed lines represent the standard deviation of the component. The standard deviation normalized by the dynamic range is given in the upper right corner of each subfigure. Here $T_N = 100$ eV, $\tau = 200$ ms, $\theta = 20^\circ$ and $N_\alpha = 0.003$. Other parameters and uncertainties are given in Table 3.1 and Table 1 respectively.

Figure 5 shows the first four of a typical set of principal components. In each subfigure the central solid line is the unperturbed classical slowing down distribution. The dotted and dash–dotted lines above and below the central line are the classical distribution plus or minus the perturbation represented by the dynamic range of the principal component [1]. The dashed lines are the distribution plus or minus one standard deviation along the

---

[1] The definition of the dynamic range of principal components is discussed in detail in BINDSLEV (1996 b). Here it is sufficient to note the graphical representation of the range given in Figure 5. The relative errors, and hence the signal to noise ratios for principal components, refer to the absolute error in relation to the dynamic range of the principal component.

principal component and thus indicate the accuracy to which this feature is resolved. The standard deviation increases with increasing structure (number of oscillations in the perturbation to the velocity distribution). This ordering of best to worst resolved feature persists throughout the range of relevant parameters.

In Figure 6 are plotted the inverse of the normalized standard deviations, $1/\sigma_{\alpha i}$, which can be interpreted as the signal to noise levels on each of the principal components. The ratios between uncertainties in different principal components (i.e. the relative heights of the bars in Figure 6) are, like the principal components themselves, fairly constant over the range of parameters relevant for JET.

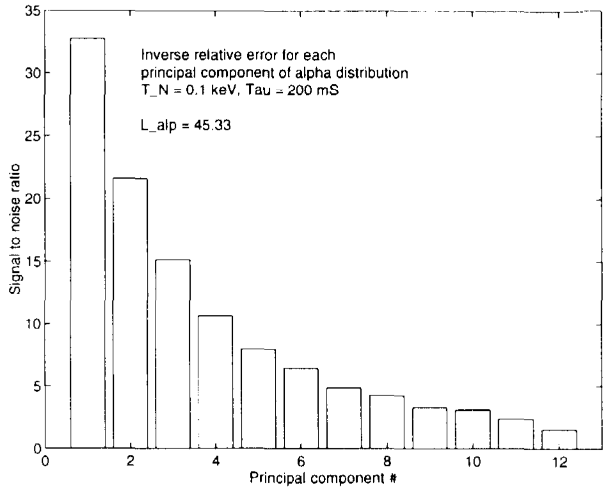

Figure 6: Inverse standard deviations, $1/\sigma_{\alpha i}$, of principal components perturbations to alpha particle distribution function. $1/\sigma_{\alpha i}$ can also be interpreted as the signal to noise ratio on the i'th principal component. Parameters are as in Figure 5.

A good measure of the ability of CTS to resolve features in the alpha particle and other fast ion distributions is the *effective signal to noise ratio*, L_α, defined as

$$L_\alpha = \left(\sum_i 1/\sigma_{\alpha i}^2 \right)^{1/2} . \tag{2}$$

L_α takes into account not only the effect of noise in the spectra but also the effect of uncertainties in constraints, masking and the sensitivity of the spectrum to variations in the fast ion distribution. L_α therefore provides a more reliable estimate of the diagnostic capability of the system than the spectral signal to noise ratio which is often quoted for CTS systems.

If we are interested in detecting departures from the classical slowdown distribution it is desirable that principal components 2 and 3 be determined with some accuracy. $L_\alpha \approx 45$ corresponds to relative errors on components 2 and 3 of respectively 5 and 7 %. This would appear to be adequate for detecting even moderate departures from the slowdown distribution. $L_\alpha \approx 10$ corresponds to relative errors on components 2 and 3 of respectively 30 and 50 %. At this level only gross departures from the slowdown distribution would be detectable. At $L_\alpha \approx 3$ no useful information on the shape of the alpha distribution function is obtained. In this case the high energy alpha density is estimated with a relative error of approximately 40 %.

L_α clearly depends on the uncertainties in the constraints, on the spectral noise, the integration time and on many other parameters. Some of these vary only slightly while variations in others have only a small impact on L_α. Here investigation of the functional dependence of L_α is limited to variations in the scattering angle, θ, and in the normalized spectral signal to noise ratio, $s = (\sqrt{\tau/100\mathrm{ms}})\,/\,(T_N/1\mathrm{keV})$, where T_N is the spectral noise temperature and τ is the total integration time. The results are displayed in Figure 7. Here we assumed the uncertainties given in Table 1 and the parameters given in Table 3.1.

Figure 7: The functional dependence of L_α on normalized spectral noise, $s = (\sqrt{\tau/100\mathrm{ms}})\,/\,(T_N/1\mathrm{keV})$, for a range of scattering angles, θ.

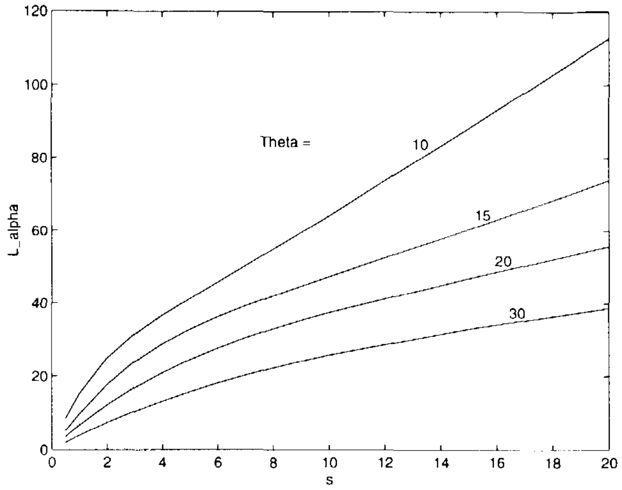

From the curves in Figure 7, L_α can be estimated for any combination of spectral noise temperature, integration time and scattering angle relevant to the CTS system at JET. The expected variation in magnetic field will have only minor effect on the spectral intensity of the scattered radiation. It will, however, significantly affect the spectral noise temperature which is investigated in the next subsection.

3.2 Spectral noise

On the basis of modelling using TRANSP on shot number 33643 it is projected that a similar shot with 50 % tritium would yield a maximum alpha density of $0.003 \times n_e$ with other parameters as in Table 3.1. For this alpha density and specified scattering angle, integration time and spectral noise temperature, L_α can be read directly from Figure 7. For instance, with a noise temperature of 1 keV and an integration time of 1 second, corresponding to $s \approx 3$, L_α would be greater than 30 for scattering angles less than 10°, making it possible to detect, in the alpha distribution, substantial departures from the classical slowdown distribution (see discussion in the previous section). At a noise temperature of 100 eV and an integration time of 0.1 second ($s = 10$) the same would be achievable with a scattering angle of 20°, and at $\theta = 15°$ L_α would be near 50 making it possible to distinguish even moderate departures from classical slowdown. Clearly a low spectral noise temperature is all important for the performance of this diagnostic. It must also be concluded that at noise temperatures above 1 keV it is virtually impossible to extract information about the shape of the alpha distribution at the projected alpha density.

The principal source of spectral noise is the electron cyclotron emission (ECE) from the plasma in the frequency range 135 GHz to 145 GHz. At moderate electron temperatures ($T_e < 5$ keV) the ECE originates from a narrow region around the cold resonance surfaces where $B = 5\,\mathrm{Tesla}/n$. Here $n = 1$ or 2 for the fundamental and the second harmonic. Figure 8 shows the locations of the cold resonances for a range of central magnetic fields.

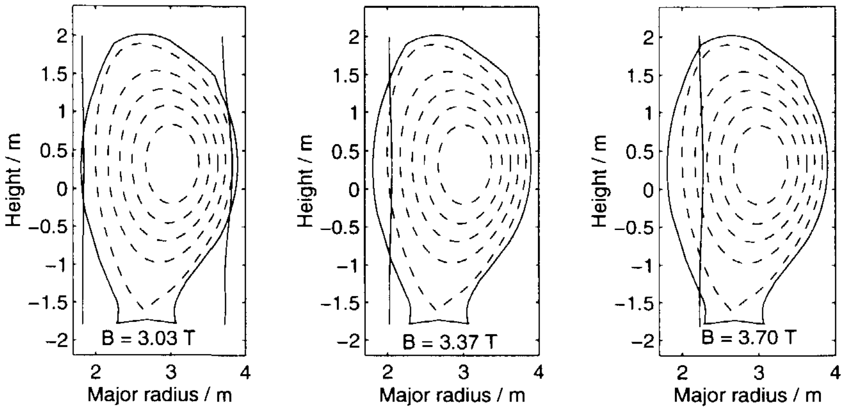

Figure 8: Locations of the cold ECE resonances for a range of magnetic fields.

The surfaces shift outward with increasing magnetic field. It is seen that from 3.1 to 3.3 Tesla both cold resonances are outside the plasma. At 3.4 Tesla the fundamental resonance enters the plasma on the inboard side. Although the receiver does not view a resonance layer directly, radiation still enters the receiver via wall reflections unless the receiver is viewing a dump. At moderate electron temperatures there would thus be a minimum in spectral noise for fields in the range 3.1 to 3.3 Tesla with a sharp rise at fields of 3.4 Tesla and above. At this minimum the noise temperature can be below 100 eV. At higher fields the noise temperature depends on plasma shape and temperature profile, but generally rises rapidly above 1 keV in the absence of a viewing dump.

At fields below 3 Tesla the second harmonic cold resonance enters the plasma from the outboard side increasing the ECE radiation and eventually blocking the receivers view of the centre of the plasma. The fields at which the cold resonances enter the plasma do of course depend on the radial extent of the plasma.

When intense ECE is emitted from a region, which is not in direct view of the receiver, substantial reduction in spectral noise temperature can be achieved by directing the receiving beam at a viewing dump. A viewing dump, for installation at the top of the torus, is presently being constructed. It will be installed with the centre of its aperture at a major radius of 3.25 metres and displaced toroidally relative to the gyrotron radiation launch mirror, to give a scattering angle of approximately 16°, with $\mathbf{k}^{\delta}$ near parallel to the magnetic field. In the absence of ECE radiation being emitted from regions in direct view of the receiver (see discussion below), this setup could reduce the spectral noise temperature dramatically, possibly to 100 eV. With an integration time of 200 ms this would yield $L_\alpha \approx 60$ implying that even moderate departures from classical slowdown in the alpha distribution would be detectable.

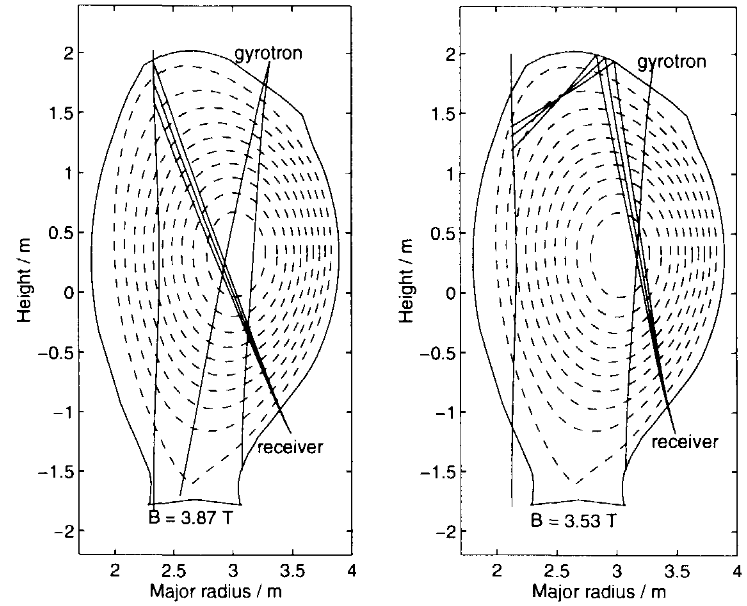

Figure 9: Scattering geometries permitting the low temperature part of the fundamental electron cyclotron resonance to be used as a viewing dump, either directly or via specular reflection in the roof tiles. Only a narrow range of poloidal angles can be used for the receiver.

An alternative approach is to use the low temperature region of the fundamental electron cyclotron resonance as a viewing dump. Two examples of how such a cyclotron viewing dump may be exploited are shown in Figure 9. In the first example the cold yet fully absorbing region of the resonance is viewed directly. In the second example the resonance is viewed after reflection in the roof tiles. The latter approach, which carries the benefit of a reduced scattering angle, depends on specular reflection in the roof tiles. Use of the cyclotron resonance as a viewing dump is only effective at fields above 3.4 Tesla, which does coincide with the fields at which the ECE emission would become unacceptably high in the absence of a beam dump. The option of using reflection in the roof tiles is not suitable at fields above 3.6 Tesla for fully elongated plasmas because the resonance is then viewed too far into the plasma. A detailed investigation by relativistic ray tracing suggests that with direct viewing the spectral noise temperature can be kept below 1 keV. The calculations are, however, very sensitive to the shape of the temperature and density profiles at the edge. The need to view a limited region of the resonance restricts the scattering geometry such that the scattering angle must be approximately 40° if the centre of the plasma is to be probed when $B = 3.53$ Tesla. Assuming $N_\alpha = 0.003$ and $\tau = 200$ ms, this results in $L_\alpha \approx 3$. If the scattering volume is placed further out at a normalized flux of 0.4 the scattering angle can be reduced to around 30° improving L_α to approximately 4. The option which makes use of reflection in the roof tiles before reaching the resonance dump generally results in slightly higher radiation temperatures (typically 1.5 keV at $B = 3.4$ Tesla) even when specular reflection is assumed. This is because of the different angle at which the dump is viewed. Non-specular reflection will increase the radiation temperature further. This geometry results in a scattering angle of approximately 15°. Assuming $N_\alpha = 0.003$ and $\tau = 200$ ms this results in $L_\alpha = 9$. These values of L_α can be improved by a little more than a factor of two by extending the integration time to the 1 second which the gyrotron is capable of.

Thus far the discussion has been confined to moderate electron temperatures ($T_e < 5$ keV). At high temperatures ($T_e > 10$ keV) an additional problem appears. Due to relativistic Doppler shift (includes non-relativistic Doppler shift and the effect of relativistically increased mass), the radiation emitted by energetic electrons is displaced from the locations of the cold resonances. In JET significant cyclotron radiation is emitted from regions displaced by a considerable fraction of the minor radius when the electron temperature is above about 10 keV. The consequence is that at 3.2 Tesla and a central electron temperature of 11 keV (as achieved in shot 33643) a strongly emitting cloud appears in the middle of the plasma resulting in a radiation temperature of 1 keV or more. This radiating cloud is downshifted second harmonic radiation.

Because this source of ECE is in direct view of the receiver, the radiation temperature cannot be reduced by any form of viewing dump. The optical thickness of the cloud, and hence intensity of radiation emitted from it, is reduce when the field is increased because the second harmonic resonance moves further out and hence fewer electrons are sufficiently energetic to radiate at the required frequency. The optical thickness of the cloud varies rapidly with temperature. For a given field there is therefore a sharp upper limit on the central electron temperature above which CTS provides little or no information on the alpha distribution. The received radiation temperature is plotted in Figure 10 as a function of central magnetic field and central electron temperature for a viewing direction which could see a dump installed in the roof. It is noted that the temperature limit increases with increasing field and decreases when viewing further out.

The central electron temperature in shot 33643, which is a model for the high performance deuterium tritium discharges, was recorded by ECE to be 12.6 keV. Modelling by relativistic ray tracing of relativistically downshifted second harmonic radiation appearing in the detected ECE spectrum suggests a central electron temperature of approximately 11.5 keV.[2] This central temperature is in accord with the estimate obtained if the the electron temperature measured by ECE is reduced to agree with the temperature measured with Lidar (the central electron temperature could not be obtained directly from lidar because it does not view the plasma centre). The electron temperature should not be expected to be less in the high performance DT discharges. This means that during the heating phase of high performance shots CTS would not benefit from a reduction of the field to 3.2 Tesla and it appears that CTS would then only provide useful information on the alpha distribution at fields of 3.4 Tesla or above. Operation under these conditions would require a viewing dump as discussed above.

An alternative approach is to take the CTS measurement in the afterglow when the main external heating has been switched off and the electron temperature has dropped.

---

[2] The hump appearing below the second harmonic in the ECE spectrum appears to be explainable as relativistically downshifted second harmonic radiation. If this is the case it may provide a good estimate of the absolute level of the temperature profile at high temperatures because from theoretical modelling this feature appears to be very sensitive to temperature. It should, however, be noted that this method of analyzing the ECE spectrum has only been conceived in connection with investigations for this report and is thus not fully developed.

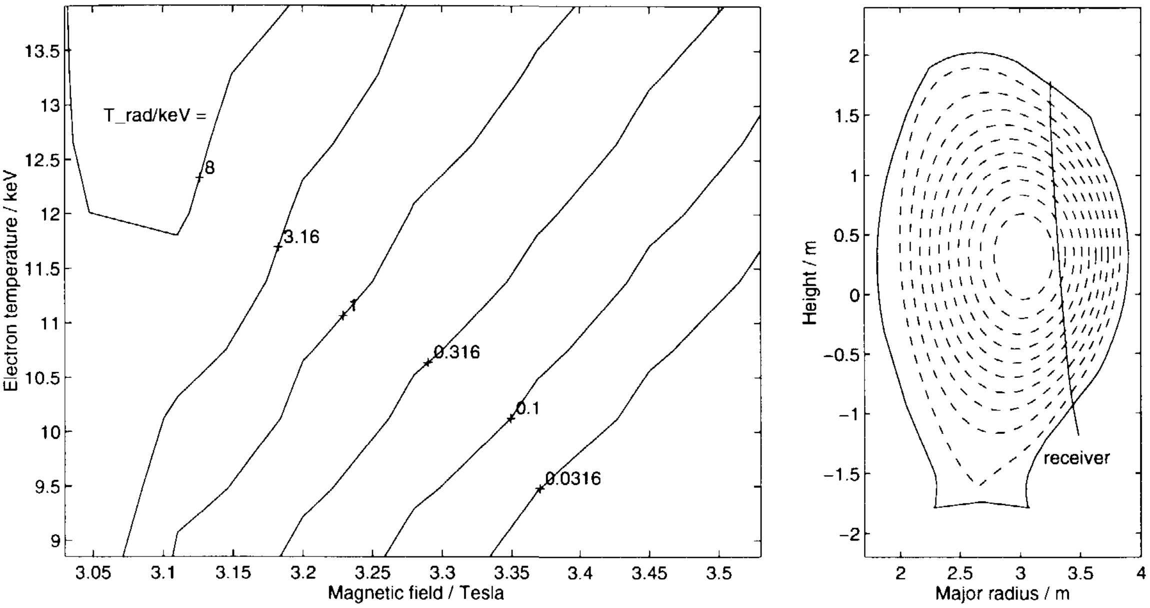

Figure 10: Temperature of received electron cyclotron radiation as a function of central magnetic field and central electron temperature. The wall is assumed cold and completely absorbing so the received radiation is emitted in direct view of the receiver. The radiation is received in O-mode at 140 GHz for a viewing direction of $\theta^s = 11^\circ$ and $\phi^s = 170^\circ$, where (θ^s, ϕ^s) are polar coordinates with vertical as the polar direction and the azimuthal angle ϕ^s being measured relative to the horizontal radial vector through the first receiver mirror. This viewing direction sees the plasma inside the $\Psi = 0.2$ normalized flux surface and the region of the roof where an artificial viewing dump could be installed. See right figure. The plasma equilibrium is based on shot 33643 at 53.3 seconds with scaled magnetic field (including the poloidal field) and scaled electron temperature.

yet before the alpha population has had time to decay significantly. On the basis of shot 33643 and TRANSP modelling it appears reasonable to assume that the electron temperature is reduced to below 8 keV in the afterglow. At this temperature there is no significant relativistically downshifted second harmonic radiation in O-mode. The intensity of radiation emitted from the cold resonance layers is, however, still significant and precautions, as discussed above, must therefore be taken also in the afterglow if a cold resonance is in the plasma, as it will be at 3.4 Tesla and above.

4 Predicted distribution of fusion alpha particles

The velocity distribution of alpha particles in devices such as JET will generally be anisotropic. Often, a significant part of the anisotropy is a consequence of the orbit motions of the fusion products. This becomes apparent when considering the expression in Kolesnichenko (1995) for the steady state velocity distribution of α-particles slowing down on electrons through Coloumb collisions.

Here, we pay special attention to the distribution function at the birth velocity v_α (E_α = 3.5 MeV). Since pitch angle scattering is negligible for particle energies above $\sim E_\alpha/10$, the anisotropy in the α distribution found at $v = v_\alpha$ is also present at lower energies. Evaluating the expression in KOLESNICHENKO (1995) with $v = v_\alpha$ for the case of a monoenergetic, isotropic source profile, $S_\alpha(\mathbf{r})$, we find:

$$f_\alpha(v_\alpha, \mathbf{r}, \chi) = \frac{1}{4\pi v_\alpha^3} \frac{\langle S_\alpha \rangle}{\langle \tau_s^{-1} \rangle} \quad , \tag{3}$$

where

$$\tau_s = \frac{3\pi^{(3/2)} \epsilon_0^2 v_e^3 m_e m_\alpha}{q_e^4 Z_\alpha^2 n_e \ln \Lambda_e} \tag{4}$$

is the Spitzer slowing down time [SPITZER 1962].

The quantities inside the angled brackets are averaged over an orbit bounce time, $\tau_b = \oint dt$:

$$\langle (\ldots) \rangle = \frac{1}{\tau_b} \int_0^{\tau_b} dt' (\ldots) \quad . \tag{5}$$

The integrations in (5) are taken along the guiding centre orbit specified by the arguments, (v_α, $\mathbf{r}$, χ), in equation (3). As we shall see the path of integration is highly dependent on the cosine of the pitch angle, $\chi = \mathbf{v} \cdot \mathbf{J}/(vJ)$, where $\mathbf{J}$ is the current. Consequently, in tokamak plasmas with inhomogeneous profiles of S_α and τ_s the distribution f_α becomes a function of χ, i.e. anisotropic.

The plasma obtained in the high performance D–D shot # 33643 in JET has been given much attention. It is hoped that the performance of this shot can be reproduced with a 50:50 Deuterium/Tritium fueling ratio in the current experimental campaign at JET. As a numerical example we have calculated f_α by using the plasma profiles measured in this shot. The Spitzer time and the orbits of integration were obtained using the profiles measured at the time of the peak performance ($t = 53.2s$). The source profile used was calculated by the TRANSP analysis code [GOLDSTON ET AL. 1981] with the assumption of a 50:50 Deuterium/Tritium fueling ratio.

In Figures 11.A and 11.B the α production rate and Spitzer time are shown as a functions of the position on the horizontal midplane at the low field side of the magnetic axis. The profiles are assumed to be functions of the flux variable. The poloidal projections of guiding centre orbits through the point $(r, Z) = (0.3, 0.0)$ are given in Figure 11.D. The trajectories correspond to different initial values of the pitch angle: $\chi \in \{-1.0, 0.9, \ldots, 1.0\}$. The distribution shown in Figure 11.C is obtained from expression (3) with $\langle S_\alpha \rangle$ and $\langle \tau_s^{-1} \rangle$ being the orbit averages over the trajectories in Figure 11.D.

In the interval $\chi \in [-1.0, -0.51]$ the α-density does not vary significantly since the trajectories corresponding to counter circulating particles are all very similar. For $\chi \in [-0.51, 0.0]$ trapped particles orbits exist. The particles contributing to the α density at

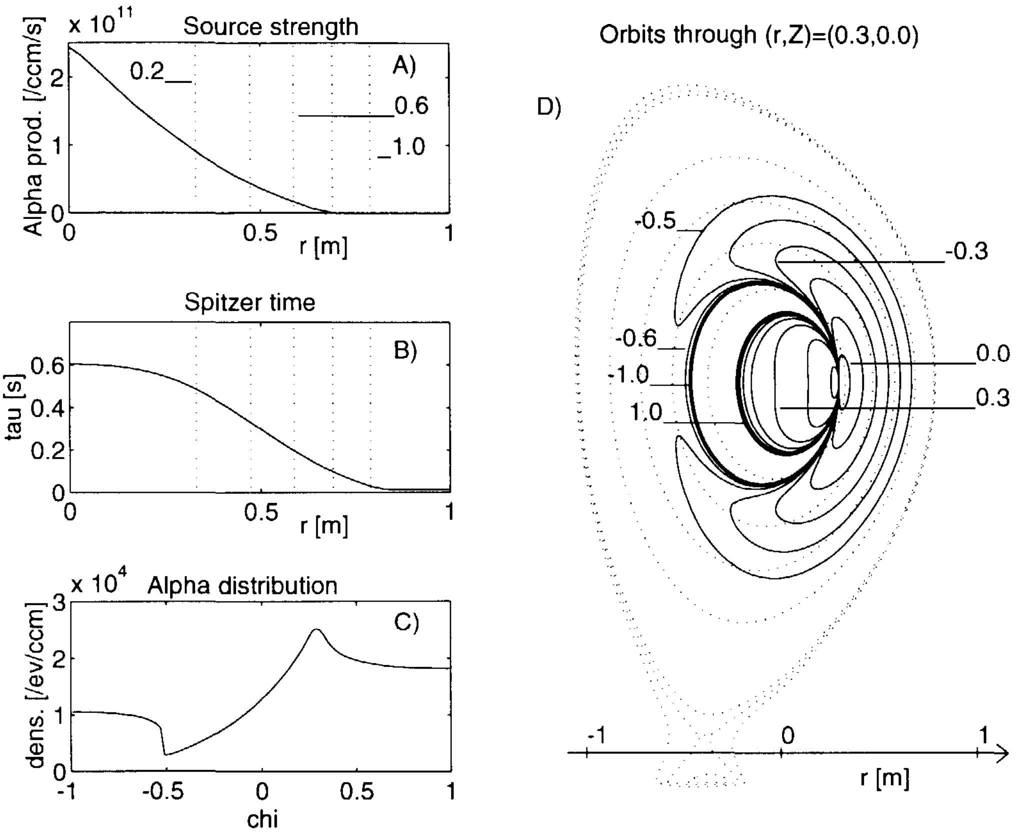

Figure 11: The graphs shown in this figure are all calculated by using the profiles measured in shot # 33643 in JET, assuming 50:50 D/T fueling ratio.

A) Profile showing the alpha particle production at the horizontal midplane.

B) Spitzer time profile on the horizontal midplane. The profiles in A) and B) are assumed to be functions of the flux variable. The positions of the flux surfaces $\Psi \in \{0.2, 0.4, 0.6, 0.8, 1.0\}$ are indicated by dotted lines.

C) Velocity distribution of α-particles at the point $r = 0.3$ on the horizontal midplane. The anisotropy seen in this distribution is closely related to the geometry of the α particle orbits through the considered point.

D) The poloidal projections of guiding centre orbits for 3.5 MeV α-particles. The trajectories correspond to values of $\chi \in \{-1.0, -0.9, \ldots, 1.0\}$. The dotted lines indicate the positions of the flux surfaces: $\Psi \in \{0.2, 0.4, 0.6, 0.8, 0.99, 1.0, 1.01\}$.

$\chi = -0.5$ are all born along the trajectory marked by -0.5 in Figure 11.D. This trajectory intersects regions with very low α–particle production which causes a low average value of the source strength. Furthermore, in the outer regions of the plasma, where the electron temperature is low, the α–particles slow down more effectively on the electrons, resulting in a short effective Spitzer time, $\langle \tau_s^{-1} \rangle^{-1}$. Hence, the density of α–particles falls dramatically at the point of transition from counter circulating orbits to trapped particle orbits ($\chi \simeq -0.50$). As χ is increased from -0.5 to 0.3 the trajectories approach the centre region. In this interval the α density increases by a factor of eight. As χ is increased further the trajectories start circulating the central region, rather than intersecting it. Consequently, as χ approaches unity the α–density decreases by a small amount from its maximal value.

Due to the differences in trajectories through different points in the plasma, the anisotropic features change with the position. In Figure 12, the distribution f_α at the horizontal midplane ($Z = 0$) is shown as a function of (r, χ). The graphs in Figure 12 indicate that even in the central region of the plasma, where there are no direct losses of α–particles to the wall, orbit effects may well introduce significant anisotropy in the velocity distribution of these particles.

The TRANSP analysis code provides a comprehensive simulation of a range of plasma parameters including the velocity distribution function for the α–particles. A TRANSP simulation was carried out for a 50:50 DT plasma where the input profiles were those measured in shot # 33643. In Figure 13 the α distributions provided by TRANSP at the positions $(r, Z) = (-0.3, 0.0)$ and $(r, Z) = (0.3, 0.0)$ are shown together with the distributions found by equation (3) at the specified locations. The α distribution in TRANSP is obtained by Monte–Carlo techniques, which introduces a significant amount of Monte–Carlo noise on the outputs. In order to limit this noise, the raw TRANSP distribution has been averaged over 0.4 s in time and integrated over the energy range 3.0–3.6MeV. The distributions calculated by TRANSP and by use of equation (3) match each other within the Monte–Carlo noise on the TRANSP distributions. The close match is remarkable considering the simplicity of the model inherent in expression (3).

The Collective Thomson Scattering diagnostic has the potential to provide spatially resolved information from which the one–dimensional distribution of ion velocities in the direction of the fluctuation wave vector, $\mathbf{k}^\delta$, may be found. One such measurement is sufficient to characterize isotropic distributions. In contrast, determination of an arbitrary three–dimensional distribution requires a large number of measurements covering virtually all directions in velocity space. The problem is considerably simplified if, as above, it is assumed that the velocity distribution is rotationally symmetric about the direction of the magnetic field, i.e. gyrotropic. In this case, with the magnetic field, $\mathbf{B}$, as the polar axis, the distribution is independent of the azimuthal angle. Directions of measurement need then only cover a range for the polar angle, $\phi = \angle(\mathbf{B}, \mathbf{k}^\delta)$. Ongoing work shows that anisotropic features may be identified with reasonable accuracy from just two measurements. A possibly surprising result is that the two directions of measurement should differ by no more than 30^0. A suitable choice for the geometry in such measurements would be $\angle(\mathbf{B}, \mathbf{k}_1^\delta) \simeq 45^0$ and $\angle(\mathbf{B}, \mathbf{k}_2^\delta) \simeq 75^0$.

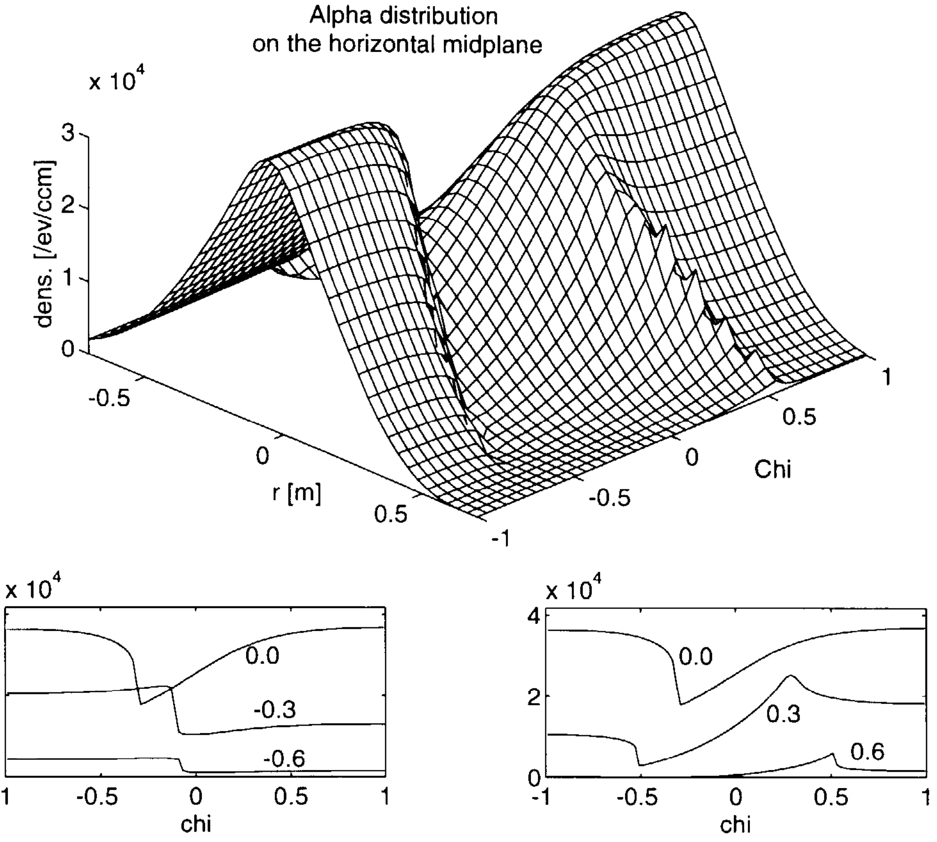

Figure 12: The alpha distribution, f_α, on the horizontal midplane as a function of position and pitch angle. The two subplots show the distribution as function of χ for $r \in \{-0.6, -0.3, 0.0, 0.3, 0.6\}$.

5 Conclusions

The initial operation of the diagnostic was useful to test the system, to demonstrate its viability and to identify areas where further improvements can be made. The results confirmed expectations and signal to noise ratios were in satisfactory agreement with theory.

Performance of the fully operational system has been assessed and compared with the needs in the coming DT campaign. This has identified a range of operational limits and the need for a viewing dump.

At the high electron temperatures expected during the heating phase of the high performance DT experiments relativistically downshifted ECE emission in direct view of the receiver makes it desirable to operate at 3.4 Tesla or above, and impossible to obtain useful alpha information at fields below 3.3 Tesla. Successful detection of the alpha distribution by CTS at such high temperatures is thus only possible at fields where the cyclotron res-

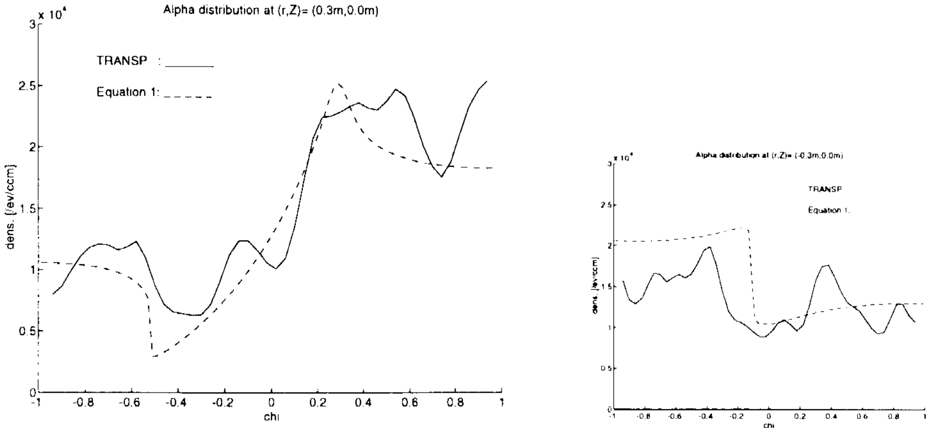

Figure 13: Velocity distributions of alpha particles at $(r, Z) = (0.3, 0.0)$ and $(r, Z) = (-0.3, 0.0)$. The full lines are obtained by TRANSP representing the distribution averaged over the energy interval [3.0, 3.6] MeV. The dashed lines, calculated by the simple model considered above, were also shown in the previous figure.

onance at 140 GHz is in the plasma, giving rise to strong ECE radiation which through wall reflections can enter the receiver. Under these conditions it is therefore necessary to operate with a viewing dump which is presently being constructed.

Finally we have shown that fast ion distributions must be expected to be anisotropic even in the case of thermonuclear fusion products with isotropic birth rates. This is to a large extent attributable to the inhomogeneous birth and slowing down rates.

References

BINDSLEV H (1993) *Plasma Physics and Controlled Fusion*, **35**, 1615.

BINDSLEV H (1995) *Proc. 7th Int. Symp. on Laser-Aided Plasma Diagnostics*, Fukuoka, Japan p. 60. (also available as JET preprint JET-P(95)66.

BINDSLEV H (1996*a*) *J. Atmospheric and Terrestrial Physics*, **58**, 983.

BINDSLEV H (1996*b*) Manuscript in preparation

COSTLEY A.E., ET.AL. (1988) JET Report R(88)08

GOLDSTON ET AL. (1981) *J. Computational Physics*, **43**, 61.

HOEKZEMA J.A., ET.AL. (1992) *Proc. 17th Int. Conf. on IR and mm Waves*, Colchester, UK pp 579, 588 and 244.

HOEKZEMA J.A., ET.AL. (1993) *Proc. 2nd Int. Workshop on Strong Microwaves in Plasmas*, Volga, Russia .

HOEKZEMA J A, ET.AL. (1995) *Proc. 22nd EPS Conference on Controlled Fusion and Plasma Physics*, Bournemouth, UK Vol. 19C, part II, p. 445. EPS JET Joint Undertaking, UK.

KOLESNICHENKO YA. (1995) *Nuclear Fusion*, **37**, 363.

SPITZER L. JR. (1962), *Physics of Fully Ionized Gases* 2nd Revised edition. Interscience, New York.